



Thermal performance of peripheral-finned tube evaporators under frosting



Marco A.S. Timmermann^a, Massoud Kaviany^b, Jader R. Barbosa Jr.^{a,*}

^a Polo - Research Laboratories for Emerging Technologies in Cooling and Thermophysics, Department of Mechanical Engineering, Federal University of Santa Catarina, Florianópolis, SC 88040900, Brazil

^b Department of Mechanical Engineering, University of Michigan, Ann Arbor, MI 48109, USA

ARTICLE INFO

Article history:

Received 29 May 2017

Received in revised form 29 July 2017

Accepted 2 September 2017

Keywords:

Peripheral finned-tube

Frost formation

Heat transfer enhancement

Heat exchanger

ABSTRACT

This study presents an experimental and theoretical evaluation of frost formation on the moist air side of a peripheral finned-tube (PFT) heat exchanger. Previous studies of this compact geometry correlated the friction and heat transfer parameters above the dew-point temperature of the air (no frost or condensate formation). Here, for the first time, the thermal-hydraulic performance of a PFT heat exchanger is analyzed under frosting. A PFT heat exchanger prototype was evaluated experimentally in a closed-loop wind tunnel calorimeter to determine the influence of the tube wall temperature, air velocity and psychrometric properties (temperature and relative humidity) on the heat transfer rate, air-side pressure drop and frost buildup on the surface. The thermal and hydrodynamic behavior of the enhanced air-side surface was analyzed using a distributed heat exchanger model in which mass, momentum and energy balances are applied to one-dimensional control volumes in the air flow direction. The model treats the air flow path as a porous medium in which the porosity, equivalent particle diameter and thermal properties vary as a function of time due to the frost accumulation. Good agreements (within 20% average error) between the model predictions and the experiments for the air-side pressure drop and heat transfer rate have been found. The enthalpy effectiveness was found to drop from 0.68 for dry to 0.50 under severe frosting, which suggests that the PFT heat exchanger continues to be effective under frost.

© 2017 Elsevier Ltd. All rights reserved.

1. Introduction

Frosting is an undesirable yet inevitable occurrence in some refrigeration and air-conditioning equipment. Different from ice, which is the result of freezing of water vapor condensate, frost originates from the desublimation of water vapor from moist air flowing over solid surfaces with temperatures below the freezing point of water. Frosting diminishes the cooling capacity and the coefficient of performance (COP) of the cooling unit by adding a low thermal conductivity resistance to the air-side surface of the evaporator, which also decreases the air flow rate due to the narrowing of the air flow passages.

Frost formation can be delayed by mechanical or chemical treatment of the heat transfer surface in order to reduce the surface energy and increase the subcooling degree required for the onset of nucleation [1,2]. Slippery liquid-infused porous surfaces [3], magnetic slippery icephobic surfaces [4] and electrically conductive surface coatings [5] have been developed to repel or

mitigate ice and frost formation. In refrigeration equipment, Joule heating is still the most common defrosting method (particularly in household systems), although several other techniques have been proposed (ultrasonic vibration, desiccant dehumidification, hot gas reverse cycle, etc.), as reviewed recently by Ref. [6].

An interesting complementary approach to any kind of frosting, icing and condensation prevention technique is the formulation of enhanced air-side geometries in such a way that the frost or condensate would appear at preferential locations (e.g., flow stagnation regions) where their accumulation would be less detrimental to the air flow distribution through the tube-fin matrix. The peripheral finned tube (PFT) concept developed by Ref. [7] consists of six radial fins connected at their tips by peripheral fins, as shown in Fig. 1. The hexagonal arrays are fabricated in three different sizes according to the length of the radial fins (R_1 , R_2 and R_3), and are arranged around the tube with an offset angle of 30° from their neighbors, forming a structured porous medium with interconnected pores. The air flows perpendicularly to the tubes. In an evaporator, the solid surfaces are colder around the tubes, so they will naturally have a bigger tendency to accumulate frost or condensate. In the PFT geometry, those regions are

* Corresponding author.

E-mail address: jrb@polo.ufsc.br (J.R. Barbosa Jr.).

Nomenclature

A	area [m ²]	w	fin width [m]
b	slope of enthalpy-temperature interpolation [J kg ⁻¹ K ⁻¹]	x	distance [m]
c_p	specific heat capacity [J kg ⁻¹ K ⁻¹]	<i>Greek</i>	
d_p	equivalent particle diameter [m]	δ	frost layer thickness [m]
f	friction factor [-]	ϵ	porosity [-]
\mathcal{G}	convective mass transfer conductance [kg m ⁻² s ⁻¹]	ϕ_{in}	relative humidity [-]
h	moist air enthalpy [J kg ⁻¹]	η_F	fin efficiency [-]
h_f	fictitious enthalpy potential [J kg ⁻¹]	η_o	overall surface efficiency [-]
h_g	enthalpy of ice [J kg ⁻¹]	ω	humidity ratio [-]
h	heat transfer coefficient [W m ⁻² K ⁻¹]	ρ	density [kg m ⁻³]
\dot{h}_{oc}	effective air-side heat transfer coefficient [W m ⁻² K ⁻¹]	<i>Subscripts and superscripts</i>	
k	thermal conductivity [W m ⁻¹ K ⁻¹]	a	dry air
K_c	contraction coefficient [-]	b	bare tube
K_e	expansion coefficient [-]	B	fin base
L	length [m]	c	coolant
Le	Lewis number [-]	cs	cross section
m	fin parameter [m ⁻¹]	CV	control volume
\dot{m}	mass flow rate [kg s ⁻¹]	F	metallic fin
M	mass [kg]	g	ice
N	number of fin arrays [-]	in	inlet
p	perimeter [m]	LM	log mean
P	pressure [Pa]	o	air-side
\dot{Q}	heat transfer rate [W]	out	outlet
t	fin thickness [m]	p	peripheral fin
τ	time [s]	r	radial fin
T	temperature [°C]	s	frost
u	in situ air velocity [m s ⁻¹]	t	total
u_D	Darcian air velocity [m s ⁻¹]		
UA	overall thermal conductance [W K ⁻¹]		
\dot{V}	moist air volumetric flow rate [m ³ s ⁻¹]		

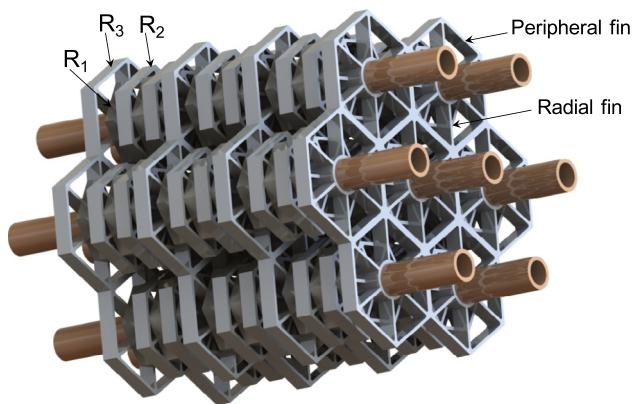


Fig. 1. The peripheral finned-tube geometry.

flow stagnation zones, so the air flow would be less disturbed by the frost growth, and would be more easily redistributed through alternative paths through the porous matrix. According to Ref. [7], the anisotropy of the porous structure also facilitates condensate drainage.

Pussoli et al. [8] performed the first experimental work on PFT heat exchangers. Five prototypes with different values of radial fin length, fin distribution and number of tube rows were tested in an open-loop wind tunnel under ‘dry’ conditions (no frost or condensate formation). A model to calculate the fin and overall surface efficiencies based on analytical expressions for the fin

temperature [7] was integrated with one-dimensional energy and momentum balances (distributed modeling approach) to compute the air-side pressure drop and air temperature in the flow direction. Good agreement between the model and the experimental data was obtained using the particle-diameter Nusselt number correlations of Whitaker [9] and Handley and Heggs [10] and friction factor relationships due to Ergun [11] and Montillet et al. [12]. Later, Pussoli et al. [13] combined entropy generation minimization with single-phase convection performance evaluation criteria (fixed geometry, fixed face area and variable geometry) [14] to determine the optimal characteristics of PFT heat exchangers.

Generally speaking, the frosting literature can be divided into studies on (i) the measurement and correlation of physical properties [15–18], (ii) the mechanisms of frost nucleation, growth and densification [19–21], and (iii) the prediction of the performance of heat exchangers under frosting [22–25]. In the latter category, the proposed distributed models are such that the air-side flow path can be divided into one-dimensional (lengthwise) or two-dimensional (lengthwise and spanwise) control volumes onto which mass, momentum and energy balances are applied to calculate the local rates of frost formation (vapor desublimation), heat transfer and the pressure drop. The local rates are integrated over the entire area of the heat exchanger to give the overall instantaneous rates. Moreover, in two-dimensional approaches, it is possible to evaluate more precisely the influence of the refrigerant flow distribution and predict the zones of the air-side surface that are more affected by the frost accretion, which has a direct impact on the air flow distribution [22,23]. Thermal capacity effects of the frost layer are usually neglected with satisfactory results in

distributed models [26]. A study of frost growth and densification in a plain fin-tube heat exchanger using Computational Fluid Dynamics (CFD) has been presented recently in Ref. [27].

The majority of heat exchanger frosting models has been proposed for *conventional* finned surfaces (e.g., integral fins, plain continuous fins, wavy fins, etc.) [22,25,27–30]. As far as the present authors are aware, no model has been proposed to predict the performance of novel (structured or unstructured) enhanced surfaces. Therefore, the objective of the present paper is to extend the analysis of Pussoli et al. [8] to predict the behavior of the PFT heat exchanger under frosting. To this end, experiments have been conducted using one of the prototypes developed in Ref. [8] in a closed-loop wind tunnel calorimeter specially designed and built for thermal-hydraulic experiments in the presence of frosting. A one-dimensional distributed heat exchanger model was developed and implemented to predict the time-dependent behavior of parameters such as the heat transfer rate, enthalpy effectiveness, pressure drop and mass of frost accumulated with time. The majority of the experimental data was predicted to within 20% deviation with respect to the data.

2. Experimental work

2.1. Heat exchanger prototype

The heat exchanger prototype evaluated in this work is shown in Fig. 2. The outer diameter of the copper tube is 8.94 mm. A staggered tube array with a mixed-mixed cross-parallel flow configuration was used. The basic dimensions of the heat exchanger and peripheral fins are shown in Table 1. The fins were made of aluminum. The fin structure is composed of three distinct levels of fin arrangement (R_1 , R_2 and R_3), each characterized by the length of the radial fin extending from the tube, as seen in Fig. 2(a). The fins were assembled with a 30° offset from their neighbors, according to the distribution shown in Table 1. Each group of six fins comprises a so-called unit, as illustrated in Fig. 2(b).

2.2. Experimental facility

The experimental tests were carried out in a closed-loop wind-tunnel calorimeter [24], as shown in Fig. 3. The apparatus controls the air flow rate and its psychrometric condition (temperature and humidity) at the test section inlet. In the lower part of the wind tunnel, the air flow is measured using a calibrated nozzle (1) connected to a differential pressure transmitter with an uncertainty of

Table 1
Characteristics of the prototype used in the tests (without frosting).

$R_1/R_2/R_3$ radial fin length [mm]	12.1/9.0/7.0
$R_1/R_2/R_3$ number of fins [-]	180/120/70
Fin thickness/ width [mm]	0.8/4.0
Fin distribution [-]	$R_3, R_1, R_2, R_1, R_2, R_1, R_3$
Porosity [-]	0.877
Number of units per tube [-]	6
Surface area [m^2]	0.826
Tube rows in the flow direction [-]	5
Matrix Height/Length/Width [mm]	63.6/128.6/148.0

$\pm 0.5\%$ of the full-scale (1744 Pa). The air is then cooled by a coil (2) connected to a vapor compressor refrigeration system (see Fig. 4). Next, the air is re-heated by an electric heater (3) and re-humidified by a water tray (4). The air flow rate is supplied by a computer-driven variable-speed centrifugal fan (5). In the upper part, a wire mesh was used to make the flow uniform at the inlet of the test section. The air temperature was measured by eighteen thermocouples (TT) (a grid with nine thermocouples at the inlet and another nine at the outlet), with an uncertainty of $\pm 0.2^\circ\text{C}$. The thermocouples were embedded into small copper blocks (diameter and height of 10 mm) to minimize temperature oscillations. The air relative humidity was measured by two humidity transducers placed upstream and downstream of the test section (HT) (uncertainty of $\pm 1\%$). The air-side static pressure drop was measured by a differential pressure transmitter (PT) with an uncertainty of $\pm 0.5\%$ of the full-scale (996 Pa).

The coolant (a water-glycol solution) temperature and flow rate are set by a secondary flow loop connected to a commercial chiller. The flow rate is measured with a turbine flow meter with an accuracy of 0.3% of the full scale ($0.68\text{ m}^3/\text{h}$). The inlet and outlet temperatures are measured by T-type immersion thermocouples ($\pm 0.2^\circ\text{C}$). The tubes that connect the heat exchanger to the chiller are thermally insulated. A schematic diagram of the flow loops is shown in Fig. 4.

2.3. Experimental procedure and test conditions

The heat exchanger is fastened onto a wooden frame inside the test section. The desired test conditions (flow rates, inlet humidity and temperatures) are adjusted in the control system. While these conditions are not reached and stabilized (usually 3 h are needed), the air and the coolant streams by pass the evaporator to avoid premature frost formation on the air-side surface [31]. The room

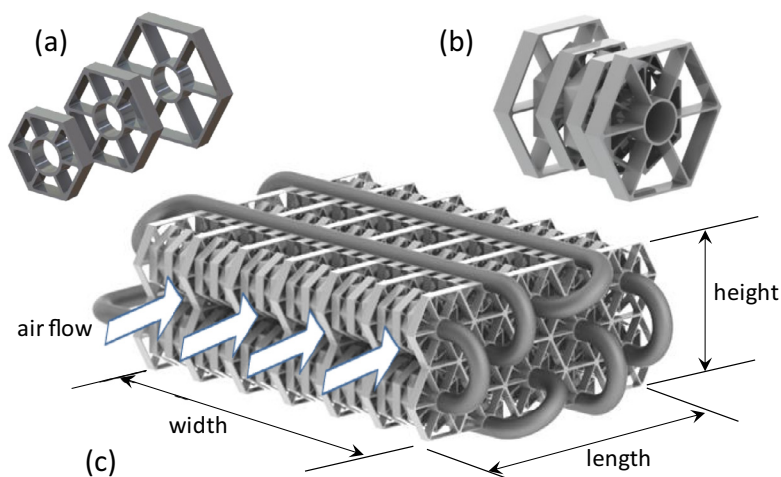


Fig. 2. (a) Fin level: 1, 2, 3. (b) Fin unit: $R_3, R_1, R_2, R_1, R_2, R_1, R_3$. (c) Heat exchanger prototype.

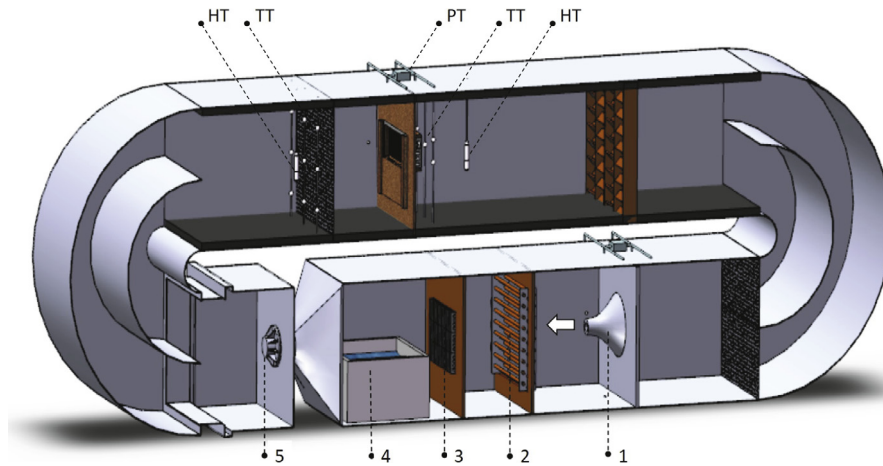


Fig. 3. Schematic diagram of the wind-tunnel calorimeter [24].

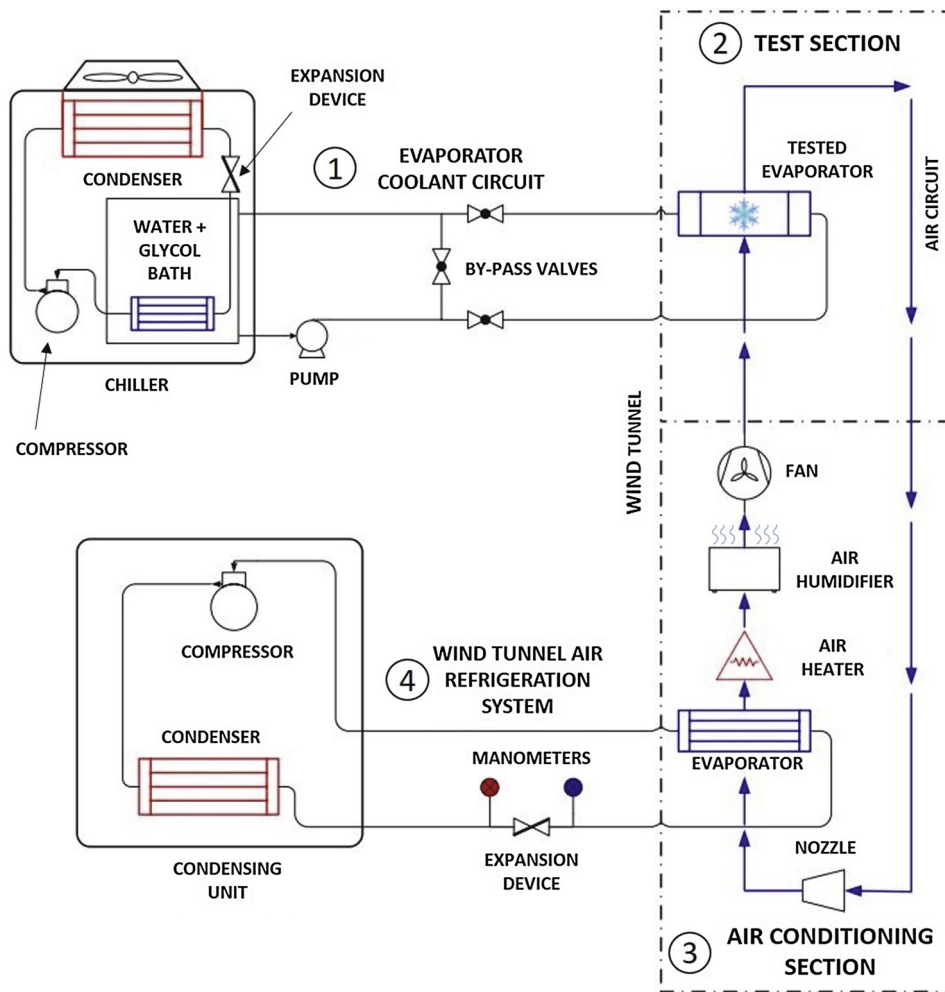


Fig. 4. Schematic diagram of the flow loops.

temperature was kept at 15 ± 1 °C. The test is started by directing the air and coolant streams to the evaporator (shutting the by pass) and beginning the data acquisition. At the end of a test, the evap-

orator is removed from the test section and placed on a tray to collect and weigh the accumulated frost on a digital scale with an accuracy of 0.01 g (gravimetric method).

In total, 24 tests were carried out with the following (nominal) conditions: inlet air flow rate: 34 and 51 m³/h; inlet air temperature: 15 °C; inlet coolant temperature: –10 °C and –15 °C; inlet relative humidity: 50% and 80%; test duration: 30, 60 and 90 min.

2.4. Data regression

The desublimation rate, \dot{m}_s , was calculated based on a moisture mass balance on the air side as follows:

$$\dot{m}_s = \dot{m}_a(\omega_{out} - \omega_{in}), \quad (1)$$

where the humidity ratios were computed based on the local measurements of air temperature and relative humidity at the inlet and outlet of the test section. In addition to the gravimetric method, the mass of frost accumulated on the air side can be computed from the integration of Eq. (1) over the duration of the test:

$$M_s = - \int_0^t \dot{m}_s dt. \quad (2)$$

The energy balance is calculated in both air and coolant sides. On the air side, the following equation:

$$\dot{Q} = \dot{m}_a(h_{out} - h_{in}) - \dot{m}_s h_g, \quad (3)$$

is used to determine the heat transfer rate. On the coolant side, there is only sensible heat transfer (no phase change of the brine). Thus,

$$\dot{Q}_c = \dot{m}_c c_{p,c}(T_{c,in} - T_{c,out}). \quad (4)$$

Fig. 5 presents the air-side heat transfer rate plotted against the heat transfer rate on the coolant side, for the entire data set. To satisfy the energy balance in the test section, the results obtained on both sides must match. Although there is no clear bias in the dataset towards a particular side (which would indicate some sort of systematic error), there is a significant random component in the data, which is responsible for most of the data points to lie within 10% error. It is believed that this scatter in the data – not usually observed in sensible heat transfer tests [32] – is somewhat related to the transient nature of the experiments.

The above mentioned transient characteristics are such that, when the air and coolant by passes are closed and the data acquisition starts – a necessary procedure to avoid premature frost formation prior to the beginning of each test – the heat exchanger and the coolant inside the tubes are still at the air temperature (15 °C). Because of that, a few minutes are necessary until the heat exchanger cools down and the equilibrium conditions are reached.

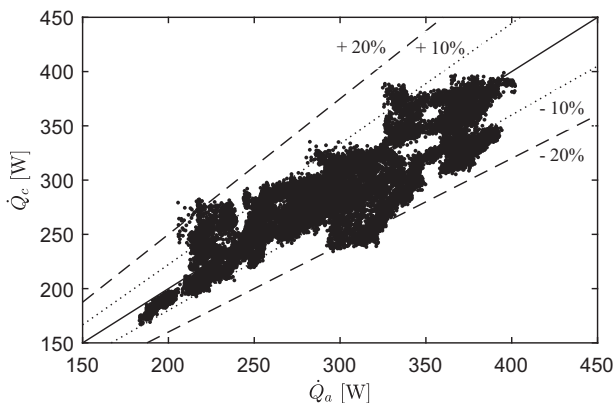


Fig. 5. Comparison between the heat transfer rates on the air and coolant side for the entire data set.

This results in lower heat and mass transfer rates during the early minutes compared to an ideal condition in which the heat exchanger is already at the lowest possible temperature at the beginning of the test. As a result, a lower mass of frost is accumulated.

Fig. 6(a) presents an example of the transient behavior of the outlet air enthalpy for a typical test. As can be seen, the outlet air enthalpy is high at the beginning, but quickly drops until a minimum value is reached. As time passes, this enthalpy slowly increases due to the frost layer thermal resistance, which reduces the heat transfer rate. Fig. 6(b) presents the outlet coolant temperature as a function of time for the same test condition. An opposite behavior can be noticed, i.e., the temperature is lower at the beginning, reaches a maximum and decreases continuously as frost builds-up.

3. Modeling

The model is divided in three parts, namely the frost formation and growth model, the fin heat transfer model and the distributed heat exchanger model. Due to the different time scales of the frost growth (longer) and air flow through the porous medium (shorter), the time dependent nature of the problem has been considered only in the frost formation and growth model. The remaining models were treated as quasi-steady. The following additional assumptions have been adopted: (i) the frost density and thickness on each extended surface (R1, R2 and R3) and on the bare tube are uniform, (ii) no air flows through the frost layer, (iii) the diffusion of heat and mass in the frost layer is one-dimensional and quasi-steady, (iv) the air flow is uniformly distributed in the spanwise direction through the heat exchanger, (v) there are no air flow by pass streams, (vi) the Lewis analogy between heat and mass convection in the moist air is valid.

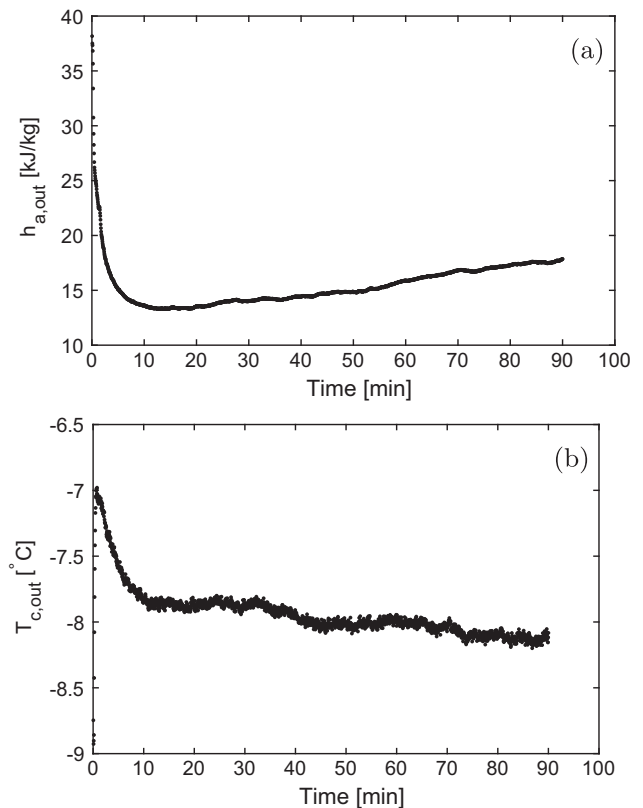


Fig. 6. (a) Outlet air enthalpy change as a function of time. (b) Outlet coolant temperature as a function of time. Experimental conditions: (a) air flow rate: 34.4 m³/h; $T_{c,in} = -10.4$ °C; $\phi_{in} = 80.2\%$; $T_{a,in} = 14.8$ °C; test duration: 90 min.

3.1. Fin heat transfer model

The basic geometry of the peripheral fins is shown in Fig. 7(a). From a symmetry argument, each hexagonal fin is a combination of six identical units formed by one radial and two halves of a peripheral fin, the so-called T-unit, shown in Fig. 7(b). Thermal equilibrium is assumed at the connection between the tip of a radial fin and the bases of two peripheral fins [7]. Thus,

$$\dot{Q}_{r,L_r} = 2\dot{Q}_{p,B} \tag{5}$$

The heat transfer rate through a frosted fin can be calculated based on the concept of fictitious fin enthalpy. Thus, an energy balance in a generic frosted fin (radial or peripheral) gives [33]:

$$\frac{d^2 \Delta h_f}{dx^2} - m^2 \Delta h_f = 0, \tag{6}$$

where the fictitious fin enthalpy potential is defined as the difference between the enthalpy of moist air, h , and the enthalpy of saturated air at the mean fin temperature. The fin parameter is given by:

$$m^2 = 2h_{oc}/(k_F t_F), \tag{7}$$

where h_{oc} is an effective heat transfer coefficient that accounts for the heat conduction in the frost layer [33]:

$$\frac{1}{h_{oc}} = \frac{c_p}{b h_o} + \frac{\delta}{k_s}, \tag{8}$$

where $b = (h - h_s)/(T - T_s)$ is the slope of the linear interpolation of the saturated air enthalpy with respect to temperature [33].

The radial and peripheral fins (differentiated from this point onward by the subscripts r and p) are subjected to different boundary conditions. For radial fins, $\Delta h_{f,r}(x = 0) = \Delta h_{f,r,B}$ (fictitious enthalpy prescribed at the base) and $\Delta h_{f,r}(x = L_r) = \Delta h_{f,r,L_r}$ (fictitious enthalpy prescribed at the tip). For peripheral fins, $\Delta h_{f,p}(x = 0) = \Delta h_{f,p,B}$ (fictitious enthalpy prescribed at the base) and $d\Delta h_{f,p}(x = L_p)/dx = 0$ (symmetry).

Solving Eq. (6) for the radial and peripheral fins with their respective boundary conditions, and using Fourier's law to determine the heat transfer rates in Eq. (5) gives:

$$\dot{Q}_{r,L_r} = \frac{k_F A_{cs}}{b_b} \left[\frac{\Delta h_{f,r,B} m_r - \Delta h_{f,r,L_r} m_r \cosh(m_r L_r)}{\sinh(m_r L_r)} \right], \tag{9}$$

$$\dot{Q}_{p,B} = \frac{k_F A_{cs}}{b_b} \Delta h_{f,p,B} m_p \sinh(m_p L_p). \tag{10}$$

where the fin parameters m_r and m_p are calculated from Eq. (7) using their respective effective heat transfer coefficients, $h_{oc,r}$ and $h_{oc,p}$, which are not equal to each other due to the different (average) frost layer thickness and thermal conductivity on each fin type. By substituting Eqs. (10) and (9) in Eq. (5), the fictitious fin enthalpy, h_f , that satisfies the equilibrium condition at the connection between the fins and the enthalpy potential distributions along them can be determined. The term b_b will be defined below.

The total heat transfer rate through an hexagonal set is given by the summation of the heat transfer rate at the base of each radial fin, $\dot{Q}_{r,B}$, and the heat transfer rate at the bare tube area, \dot{Q}_b :

$$\dot{Q} = 6 \dot{Q}_{r,B} + \dot{Q}_b, \tag{11}$$

where \dot{Q}_b can be calculated using a convective enthalpy potential relationship as follows:

$$\dot{Q}_b = \frac{h_{oc,b}}{b_b} A_b (h - h_{f,b}), \tag{12}$$

where b_b is the slope of the linear interpolation of the saturated air enthalpy with respect to the temperature of the frost surface in the bare tube area, $b_b = (h - h_{s,b})/(T - T_{s,b})$. The latter temperature was chosen as a reference in the interpolations associated with all other fins (Eqs. (9) and (10)) because it is the lowest air temperature in the computational domain.

The heat transfer rate at the base of a radial fin is calculated based on the derivative of the temperature profile at $x = 0$. $\dot{Q}_{r,B}$ is also equal to the total heat transfer rate in a T-unit, which can be written in terms of a convective heat transfer relationship. Thus:

$$\dot{Q}_{r,B} = \frac{k_F A_{cs}}{b_b} \left[\frac{\Delta h_{f,r,B} m_r \cosh(m_r L_r) - \Delta h_{f,r,L_r} m_r}{\sinh(m_r L_r)} \right] = \frac{h_{oc} A_F}{b_b} (h - h_{f,B}) \eta_F. \tag{13}$$

After some algebraic manipulation of the above equation, it is possible to obtain a relationship for the fin efficiency of the T-unit as follows:

$$\eta_F = \left(\frac{p_F k_F A_{cs}}{h_{oc} A_F^2} \right)^{1/2} \frac{\left[\cosh(m_r L_r) - \frac{h - h_{f,L_r}}{h - h_{f,B}} \right]}{\sinh(m_r L_r)}, \tag{14}$$

where $p_F \approx 2w_F$ and $A_{cs} = w_F t_F$.

Replacing Eqs. (12) and (13) in Eq. (11), and assuming that $h_{oc} \approx h_{oc,b}$ gives:

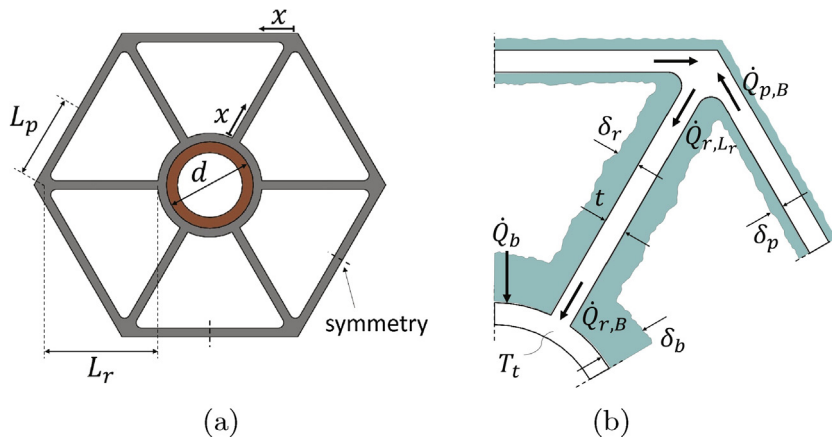


Fig. 7. Geometry of the peripheral fins (a) basic dimensions, (b) a T-unit (covered by a frost layer).

$$\begin{aligned}\dot{Q} &= 6 \eta_F \dot{h}_{oc} A_F \left(\frac{h - h_{f,B}}{b_b} \right) + \dot{h}_{oc,b} A_b \left(\frac{h - h_{f,B}}{b_b} \right) \\ &= \dot{h}_{oc} A_t \eta_o \left(\frac{h - h_{f,B}}{b_b} \right),\end{aligned}\quad (15)$$

where $A_t = A_b + 6A_F$ is the total surface area of the hexagonal set. The overall surface efficiency is:

$$\eta_o = 1 - \frac{6 A_F}{A_t} (1 - \eta_F). \quad (16)$$

3.2. Distributed heat exchanger model

To calculate the total heat transfer rate, pressure drop and desublimation rate, the evaporator is divided into uniform control volumes in the direction of the air flow, as shown in Fig. 8. The number of control volumes in the one-dimensional distributed model, N_{CV} , coincides with the number of tube rows (five) in the flow direction [8]. The air flow is assumed to be uniformly distributed in the spanwise direction.

Energy balances between the inlets and outlets of the moist air and coolant streams of a given control volume are given by:

$$\dot{Q}_{CV} = \dot{m}_a (h_{in} - h_{out}) - \dot{m}_{s,CV} h_s = -\dot{m}_c (h_{c,out} - h_{c,in}). \quad (17)$$

The heat transfer rate in a control volume can be calculated based on the concept of log-mean enthalpy difference as follows [33]:

$$\dot{Q}_{CV} = UA_{CV} \Delta h_{LM,CV} = UA_{CV} \left[\frac{(h_{in} - h_{fc,out}) - (h_{out} - h_{fc,in})}{\ln \left(\frac{h_{in} - h_{fc,out}}{h_{out} - h_{fc,in}} \right)} \right], \quad (18)$$

where $h_{fc,in}$ and $h_{fc,out}$ are the fictitious enthalpies of the coolant at the inlet and outlet of the control volume. The total heat transfer rate can be calculated by adding the contributions of the N_{CV} control volumes. The overall heat transfer coefficient associated with each control volume is given by (neglecting the conduction resistance of the tube wall):

$$\frac{1}{UA_{CV}} = \frac{b_c}{\dot{h}_i A_i} + \frac{b_b}{\sum_{k=1}^3 N_k \dot{h}_{oc,k} A_{o,k} \eta_{o,k}}, \quad (19)$$

where $b_c = (h_{f,s} - h_{f,c}) / (T_s - T_c)$ and T_c is the average coolant temperature in the control volume [33]. In Eq. (19), k is a counter for the number of fin array types, so $k = 1$ corresponds to level R_1 , $k = 2$ to level R_2 and $k = 3$ to level R_3 . N_k is the number of fin arrays of the k th type in the control volume. η_o is the overall efficiency of the (frosted) finned surface (Eq. (16)). A_i is the internal surface area (tube) and A_o is the external surface area, which

includes the area of the frosted fins and frost-covered bare tube, as seen in Fig. 7(b). The internal heat transfer coefficient, \dot{h}_i , was estimated using the Gnielinski correlation when the flow was in the turbulent regime [34]. The air-side heat transfer coefficient, $\dot{h}_{oc,k}$, was estimated using the Handley and Heggs [10] correlation. Although \dot{h}_o is considered the same for all fins in a given control volume, the effective heat transfer coefficient, $\dot{h}_{oc,k}$, calculated from Eq. (8), is different for each fin type because of the different values of frost layer thickness and thermal conductivity. Also, while the first and second terms on the right hand side of Eq. (19) are thermal resistances connected in series (in-tube and air-side convection), the individual components in the denominator of the latter term (associated with each fin level) are thermal resistances connected in parallel.

The water vapor desublimation rate is calculated based on a species mass balance between the inlet and the outlet of each control volume,

$$\begin{aligned}\dot{m}_{s,CV} &= \dot{m}_a (\omega_{in} - \omega_{out}) \\ &= \mathcal{G}_o \left(\sum_{k=1}^3 A_{p,o,k} \Delta \omega_{LM,p,k} N_{p,k} + \sum_{k=1}^3 A_{r,o,k} \Delta \omega_{LM,r,k} N_{r,k} + A_{b,o} \Delta \omega_{LM,b} \right),\end{aligned}\quad (20)$$

where in each control volume \mathcal{G}_o is calculated using the Lewis analogy between convective heat and mass transfer on the air side, $\mathcal{G}_o = \dot{h}_o / c_p L e^{2/3}$ [35]. $\Delta \omega_{LM,j,k}$ is the log-mean humidity ratio given by:

$$\Delta \omega_{LM,j,k} = \frac{(\omega_{in} - \omega_{sat,j,k}) - (\omega_{out} - \omega_{sat,j,k})}{\ln \left(\frac{\omega_{in} - \omega_{sat,j,k}}{\omega_{out} - \omega_{sat,j,k}} \right)}. \quad (21)$$

which defines the mass transfer driving potential for frost formation. Analogous definitions have been used by other authors [20,36].

In a control volume, each fin type ($j = r$ or p), in each level (R_1 , R_2 or R_3), has its own fictitious enthalpy distribution, resulting in different mean surface temperatures (and different corresponding saturation humidity ratios). Hence, there are different log-mean humidity ratios for each fin and bare-tube parts, resulting in seven different contributions to the overall desublimation rate in each control volume. Again, the total vapor desublimation rate is calculated adding the rates associated with each control volume.

The total air-side pressure drop is calculated as follows:

$$\begin{aligned}\Delta P &= \frac{1}{2} \rho_1 u_1^2 (1 - \epsilon_1^2 + K_c) + \sum_{n=1}^{N_{CV}} f_n L_n \frac{\rho_n u_{b,n}^2 (1 - \epsilon_n)}{d_{p,n}} \\ &\quad - \frac{1}{2} \rho_{N_{CV}} u_{N_{CV}}^2 (1 - \epsilon_{N_{CV}}^2 - K_e)\end{aligned}\quad (22)$$

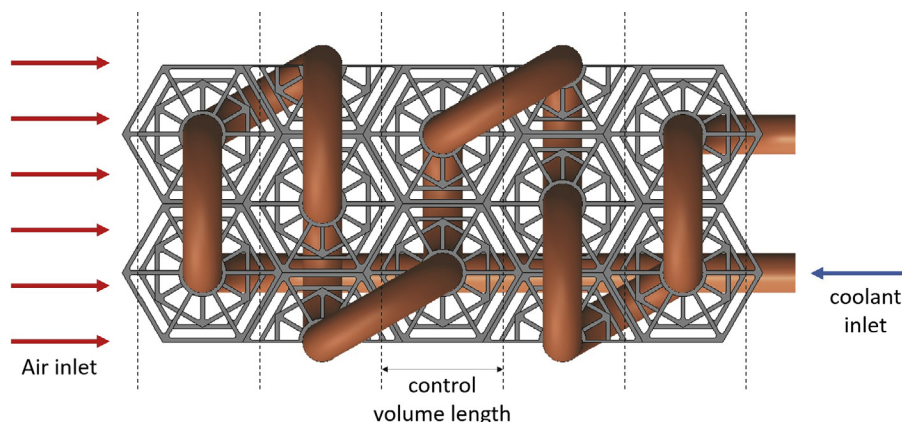


Fig. 8. Heat exchanger model geometry.

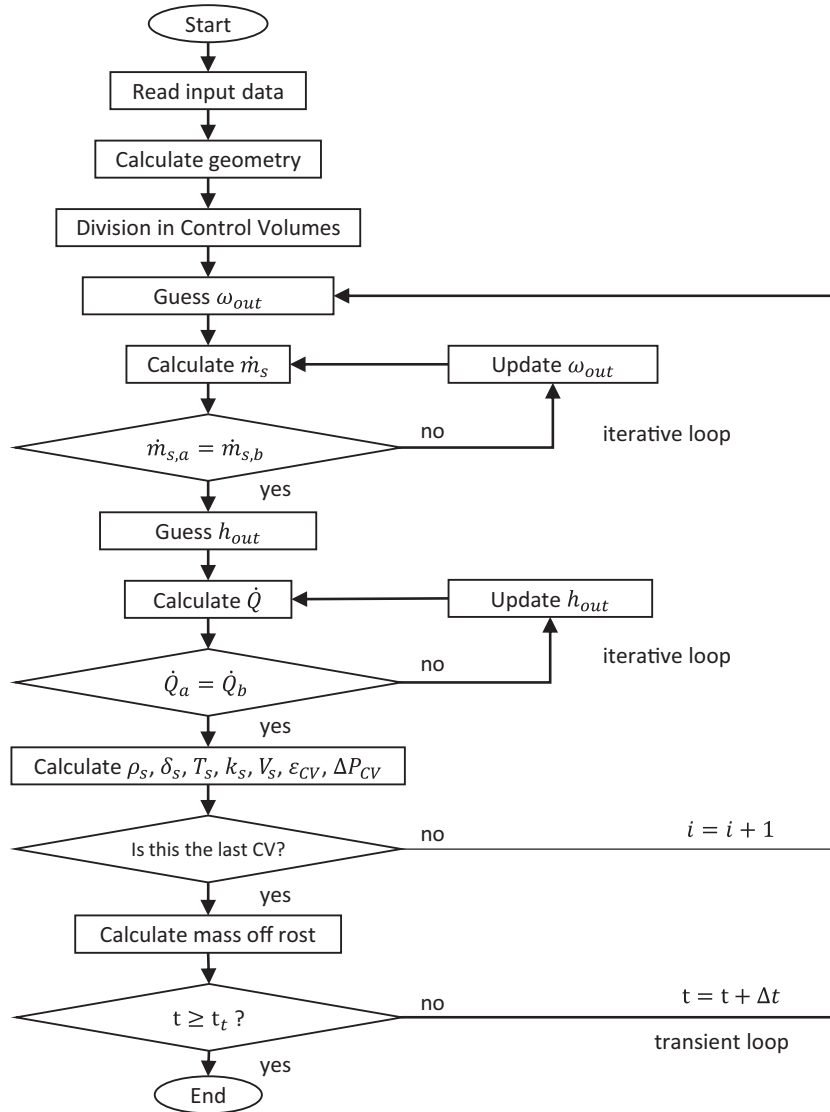


Fig. 9. Flow chart of the solution algorithm.

where the first and third terms are the entrance and exit pressure losses, respectively. The contraction and expansion coefficients, K_c and K_e , were obtained from Ref. [34], assuming that the air side behaves as stack of parallel plates. u_1 and $u_{N_{CV}}$ are the in situ velocities in the first and last control volumes. The second term accounts for the frictional pressure drop (skin friction and form drag) in the $n = 1$ to N_{CV} control volumes of the porous matrix. u_D is the Darcian velocity of the moist air. The equivalent particle diameter was calculated as six times the ratio of the solid volume (metal and frost) to the interstitial area. As in the heat and mass transfer calculation, five control volumes were considered. The friction factor was calculated using the Ergun [11] correlation.

3.3. Frost formation and growth model

The aim of the frost formation model is to quantify the change in frost thickness and density as a function of time on the fins of each type and level in each control volume. The assumptions of the frost formation and growth model were outlined in the introduction to Section 3. For each fin type ($j = r, p$) and level ($k = 1, 2, 3$), a frost mass balance is given by:

$$\frac{d}{dt} (\rho_{s,j,k} \delta_{s,j,k}) = \rho_{s,j,k} \frac{d\delta_{j,k}}{dt} + \delta_{j,k} \frac{d\rho_{s,j,k}}{dt} = \mathcal{G}_o \Delta\omega_{LM,j,k}, \quad (23)$$

where the first term of the center equation is due to frost growth and the second is due to frost densification. The frost density was calculated based on the correlation of Hayashi et al. [15] given by $\rho_s = 650 \exp(0.277T_s)$, where T_s is the temperature of the frost surface in °C. A linearized form of Eq. (23) is used to calculate the frost thickness at every integration time step [26].

The temperature of the frost surface on each fin is calculated through an energy balance at the interface between the frost layer and the moist air. The thermal capacity of the frost layer was neglected and a linear temperature distribution was assumed. Thus:

$$T_{s,j,k} = \bar{T}_{f,j,k} + \frac{\dot{Q}_{j,k} \delta_{j,k}}{k_{s,j,k} A_{o,j,k}} \quad (24)$$

where $A_{o,j,k}$ is the surface area of the frosted fin, $\bar{T}_{f,j,k}$ is the average fin temperature (calculated based on the fictitious enthalpy distribution) and $\dot{Q}_{j,k}$ is the total heat transfer rate through each fin. The thermal conductivity of the frost was calculated using the

empirical relationship proposed by Lee [37] as a function of the frost density.

3.4. Model implementation

The model equations were implemented on the Engineering Equation Solver (EES) [38]. The calculation starts with the data input, namely the heat exchanger geometry, the air psychrometric conditions and flow rate, the coolant temperature and flow rate and the test duration. Then, the basic geometric parameters such as the total volume and porosity are calculated. The calculations at the first control volume start by guessing the outlet humidity ratio and solving the two equalities in Eq. (20) iteratively until convergence is obtained for the vapor desublimation rate. Also, an initial guess is made for the outlet moist air enthalpy, and a similar iterative process is performed to obtain convergence of the heat transfer rate by solving together the first equality in Eqs. (17) and (18). These iterative loops were implemented in a subroutine based on Newton's method.

As the mass and heat transfer rates in the first control volume are determined, the air outlet temperature and humidity ratio and the coolant outlet temperature are carried forward as the inlet values to the next control volume. Also, other variables such as the frost density, thermal conductivity, surface temperature, thickness and volume, and the control volume porosity and pressure drop can be determined. This process is then repeated for all control volumes, for all time steps until the prescribed test duration is achieved. Lastly, the total mass of frost accumulated during the simulation is calculated. Fig. 9 shows the steps of the solution algorithm, where subscript 'a' refers to the rate variable ($\dot{m}_{s,cv}$ or \dot{Q}_{cv}) calculated from a mass or energy balance in the control volume, and subscript 'b' refers to the convective transfer rate in the control volume.

4. Results

4.1. Frost mass deposition

The behavior of the frost mass accumulated on the air-side surface is shown in Fig. 10 for two typical tests. An almost linear increase is observed in the experimental data (determined through the experimental mass balances via Eqs. (1) and (2)) and in the model predictions. This behavior was observed in all experiments, and is consistent with the experimental observations and predictions by several authors [15,25,39,40].

Similar to the heat transfer rate (to be shown later) the frost mass accumulated on the air side surface is higher in the first control volume and reduces downstream due to the decreasing mass transfer driving potential (see Eq. (23)).

The frost mass measured with a scale at the end of the test is also shown in Fig. 10. Fig. 11 compares the predictions of frost mass accumulated with the experimental data for the entire data set. Only the last data point (i.e., total mass accumulated at the end of the test, which is close to with the time when the heat exchanger was removed from the test section) is shown for the experimental air-side mass balance.

The model behaves satisfactorily (within 20% error) for values of total mass lower than 120 g, but generally under predicts the mass of frost for greater times. Regarding the experimental data only, the gravimetric results were consistently larger than those obtained via the mass balance, except for the short (30-min) tests. In these tests, the model clearly over predicted the frost mass obtained via the experimental mass balance. Because of the transient nature of the experiments, a few minutes are necessary until the equilibrium conditions are reached. In those early minutes, the

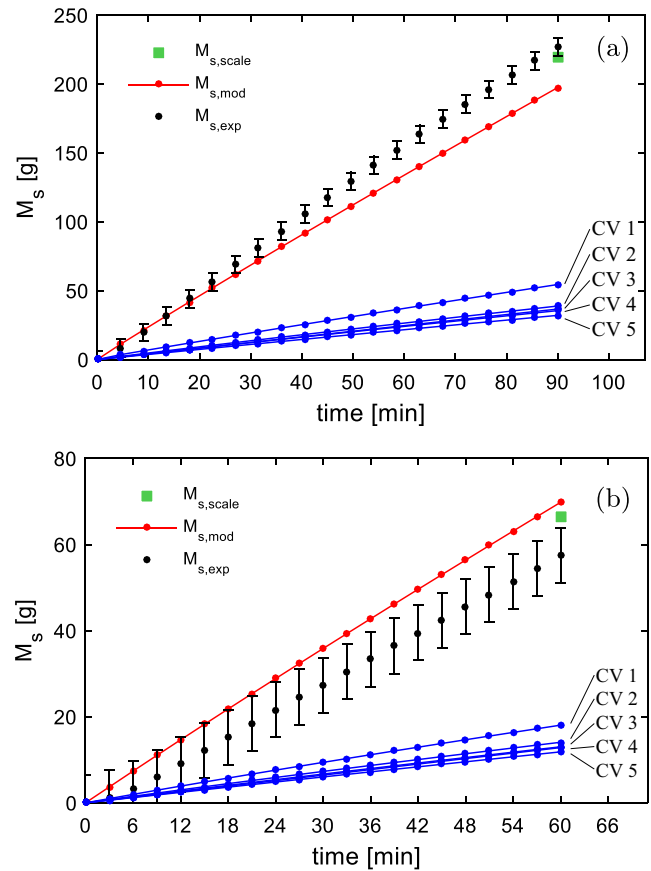


Fig. 10. Prediction of the frost mass accumulated in the heat exchanger as a function of time (overall and per control volume). Experimental conditions: (a) air flow rate: $34.4 \text{ m}^3/\text{h}$; $T_{c,in} = -10.4 \text{ }^\circ\text{C}$; $\phi_{in} = 80.2\%$; $T_{a,in} = 14.8 \text{ }^\circ\text{C}$; test duration: 90 min, (b) air flow rate: $34.4 \text{ m}^3/\text{h}$; $T_{c,in} = -10.2 \text{ }^\circ\text{C}$; $\phi_{in} = 49.4\%$; $T_{a,in} = 15.1 \text{ }^\circ\text{C}$; test duration: 60 min.

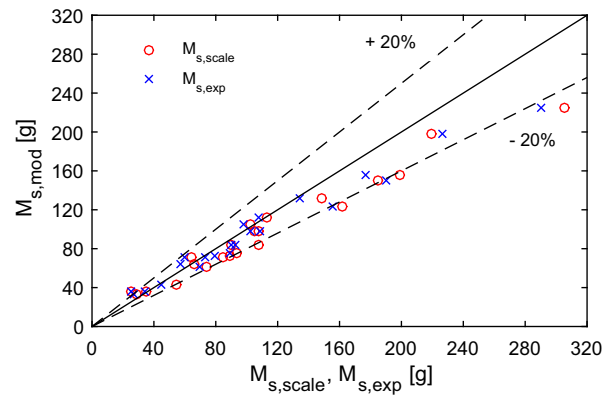


Fig. 11. Comparison between the frost accumulation predicted by the model and the experimental data.

vapor desublimation on the heat exchanger surface may not be as intense as predicted due to thermal capacity effects of the heat exchanger itself, which are neglected in the model. As a whole, the total frost mass accumulated in the heat exchanger (gravimetric results) during a test followed the expected behavior of increasing for lower values of $T_{c,in}$ and higher values of ϕ_{in} and \dot{V} , all of which result in either an increase of mass transfer driving potential or conductance.



Fig. 12. Uneven frost accumulation on the first tube rows. Arrows indicate the direction of the coolant flow inside the tube.

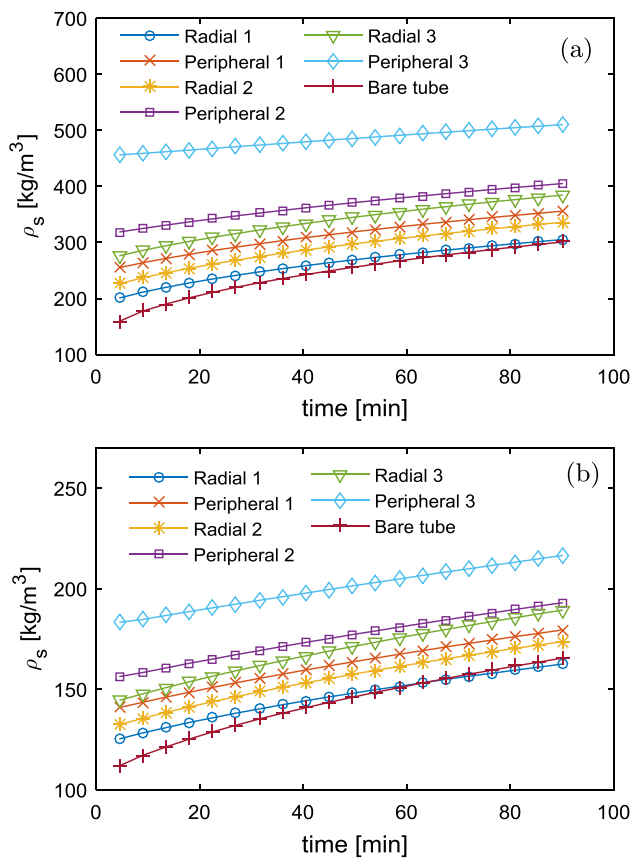


Fig. 13. Frost density temporal variation on each extended surface type in (a) CV1 and (b) CV5. (c) Average frost density (per control volume). Experimental conditions: air flow rate: $34.4 \text{ m}^3/\text{h}$; $T_{c,in} = -10.4^\circ\text{C}$; $\phi_{in} = 80.2\%$; $T_{a,in} = 14.8^\circ\text{C}$; test duration: 90 min.

In virtually every test, an uneven frost deposit was observed in the first tube row (air inlet), as presented in Fig. 12. A larger amount of frost accumulated on the right side of the top tube and on the left side of the bottom tube, which coincide with the coolant inlet of each tube pass (the arrows indicate the coolant flow direction). A smaller amount of frost is clearly observed on the opposite sides of each tube. A possible explanation for this phenomenon (also observed in Ref. [22]) lies in the existence of a coolant thermal development region downstream of the U-bends that connect each tube pass. As the local internal heat transfer coefficient is higher in this region due to flow mixing, the tube wall

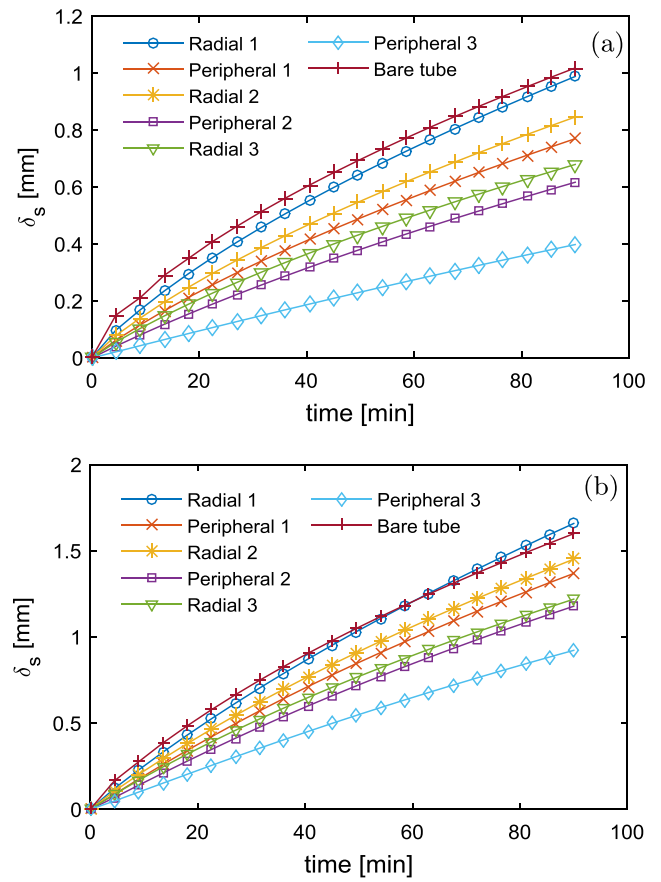


Fig. 14. Frost layer thickness temporal variation on each extended surface type in (a) CV1 and (b) CV5. Experimental conditions: air flow rate: $34.4 \text{ m}^3/\text{h}$; $T_{c,in} = -10.4^\circ\text{C}$; $\phi_{in} = 80.2\%$; $T_{a,in} = 14.8^\circ\text{C}$; test duration: 90 min.

temperature becomes closer to the bulk coolant temperature, thereby increasing the mass transfer driving potential.

Predictions of frost density and frost layer thickness on each surface type in the first and fifth control volumes (CV1 and CV5) are shown in Figs. 13 and 14 for a typical test condition. In each control volume, denser frost is formed on the surfaces with a higher temperature (further away from the tube), which is physically consistent with the correlation of Hayashi et al. [15]. As a direct consequence of the frost mass balance applied to each extended surface (Eq. (23)), the surfaces with a higher densification mass flux (second term) in comparison with the growth mass flux (first term) exhibit a smaller frost thickness (Fig. 14). The $t^{1/2}$

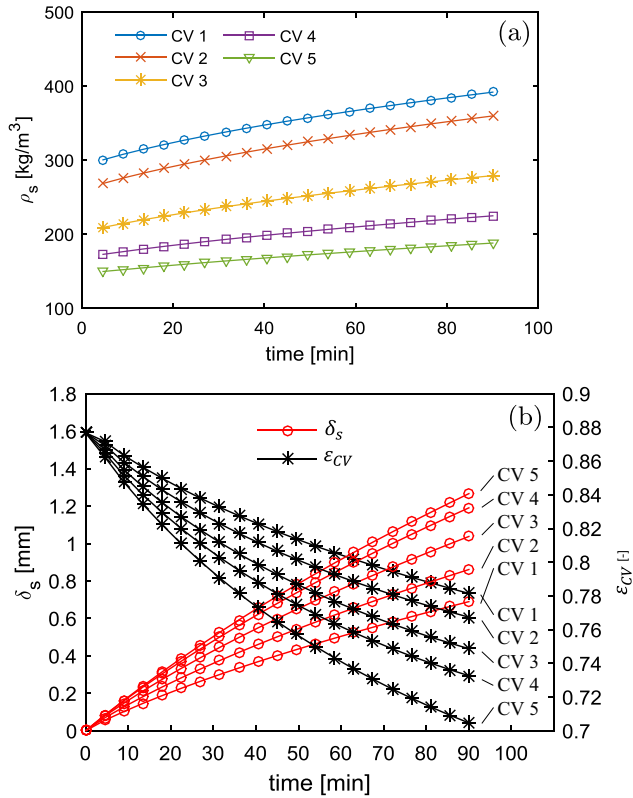


Fig. 15. Prediction of the average frost density (per control volume) as a function of time. Experimental conditions: (a) air flow rate: 34.4 m³/h; $T_{c,in} = -10.4$ °C; $\phi_{in} = 80.2\%$; $T_{a,in} = 14.8$ °C; test duration: 90 min, (b) air flow rate: 50.5 m³/h; $T_{c,in} = -10.2$ °C; $\phi_{in} = 78.6\%$; $T_{a,in} = 15.4$ °C; test duration: 90 min.

behavior of the frost thickness growth is in line with the findings of Refs. [19,21,41–43]. The average frost density per control volume (Fig. 13) also follows a similar growth trend.

The calculated average frost density and average frost layer thickness are shown in Fig. 15 for the same test condition of Figs. 13 and 14. Fig. 15(b) presents the temporal variation of the heat exchanger porosity (i.e., the volume fraction occupied by the air) in each control volume of the heat exchanger, which is inversely proportional to the frost thickness. The larger calculated frost thickness in the last control volume may seem unexpected at first. Given that the average coolant temperature is lower in the first control volume, and increases downstream, one would expect colder fins and, consequently, a thicker frost layer in CV1. However, the air average temperature is much higher near the inlet than in the subsequent control volumes. For example, in the condition shown in Fig. 15, in the last time step of the simulation, the air entered the first control volume at 14.8 °C and left it at 8.9 °C. In the last control volume, the air entered at -0.33 °C and left at -1.38 °C. As will be shown in Section 4.3, the higher air temperature in CV1 and the large air-side thermal conductance bring the average fin temperature up, which results in higher values of frost density, lower values of frost thickness and, consequently, higher heat exchanger porosities in the first control volume compared to the subsequent control volumes. Although consistent with the modeling assumptions and closure relationships used in the model, the predicted streamwise variation of the frost density and thickness requires an experimental validation.

It should be also mentioned that the change in frost surface area in contact with the moist air tends to follow the same trend of the frost thickness, but its magnitude is relatively small (less than 12% in all tests), bearing in mind the high surface area density of the

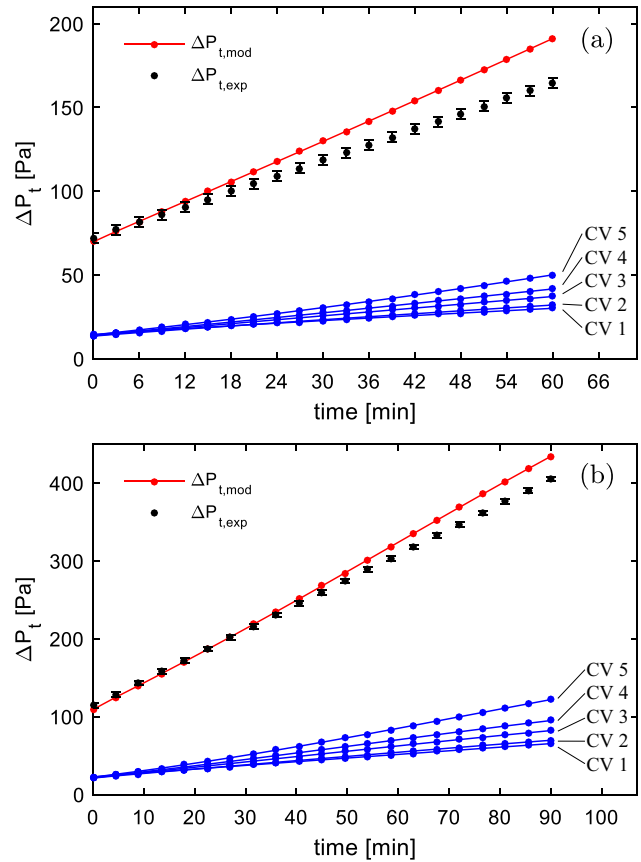


Fig. 16. Prediction of the air-side pressure drop as a function of time (overall and per control volume). Experimental conditions: (a) air flow rate: 34.4 m³/h; $T_{c,in} = -10.2$ °C; $\phi_{in} = 49.4\%$; $T_{a,in} = 15.1$ °C; test duration: 60 min., (b) air flow rate: 50.5 m³/h; $T_{c,in} = -10.2$ °C; $\phi_{in} = 78.6\%$; $T_{a,in} = 15.1$ °C; test duration: 90 min.

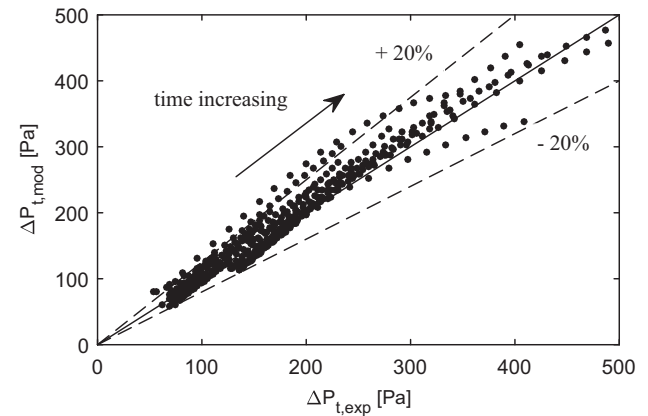


Fig. 17. Comparison between the model predictions and experimental pressure drop results for the entire data set.

heat exchanger. Therefore, considering again Eq. (23), the linear mass accumulation as a function of time observed in Fig. 10 is somehow justified. Since the frost surface area change is small and both density and frost thickness grow with the square root of time, their respective terms are counterbalanced in Eq. (23) [44].

4.2. Air-side pressure drop

Fig. 16 shows the pressure drop predictions for two typical test conditions. The agreement is better at earlier times, but still

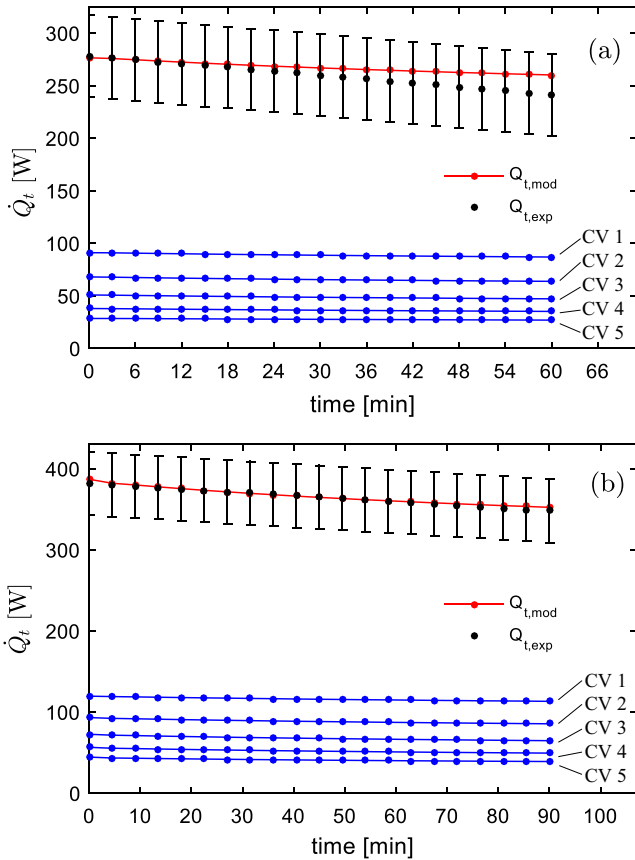


Fig. 18. Prediction of the heat transfer rate as a function of time (overall and per control volume). Experimental conditions: (a) air flow rate: 34.4 m³/h; $T_{c,in} = -10.2$ °C; $\phi_{in} = 49.4\%$; $T_{a,in} = 15.1$ °C; test duration: 60 min, (b) air flow rate: 50.5 m³/h; $T_{c,in} = -10.2$ °C; $\phi_{in} = 78.6\%$; $T_{a,in} = 15.1$ °C; test duration: 90 min.

reasonable throughout the whole experiment. Although the theoretical pressure drop is almost the same in all control volumes at the beginning of the run, the differences between them increase with time, and the pressure drop is higher in the last control volume (CV5). This is due to the increase in frost thickness (reduction of the heat exchanger porosity), which accelerates the air through the heat exchanger, as shown in Fig. 15(b).

The pressure drop results considering the entire data set are shown in Fig. 17. As in the purely sensible heat transfer (no frosting) tests of [8], the model is in good agreement with the data, with a slight tendency of under predicting the data at earlier times (lower pressure drops). At least for the conditions evaluated in the present experiments, it appears that frosting has a significant impact on the PFT heat exchanger geometry pressure drop. So, the hypothesis of Ref. [7] that frost formation would have a low impact on the PFT heat exchangers was not entirely confirmed.

4.3. Heat transfer and enthalpy effectiveness

Fig. 18 presents the temporal behavior of the heat transfer rate for two typical tests. As expected, in all test conditions the heat transfer rate decreases gradually due to the increase in thermal resistance caused by frost accumulation on the heat exchanger surface. The heat transfer rates per control volume predicted by the mathematical model are also shown. As expected, the heat transfer rate is higher in the first control volume due to the larger enthalpy difference between the air and the refrigerant, which gradually decreases further downstream.

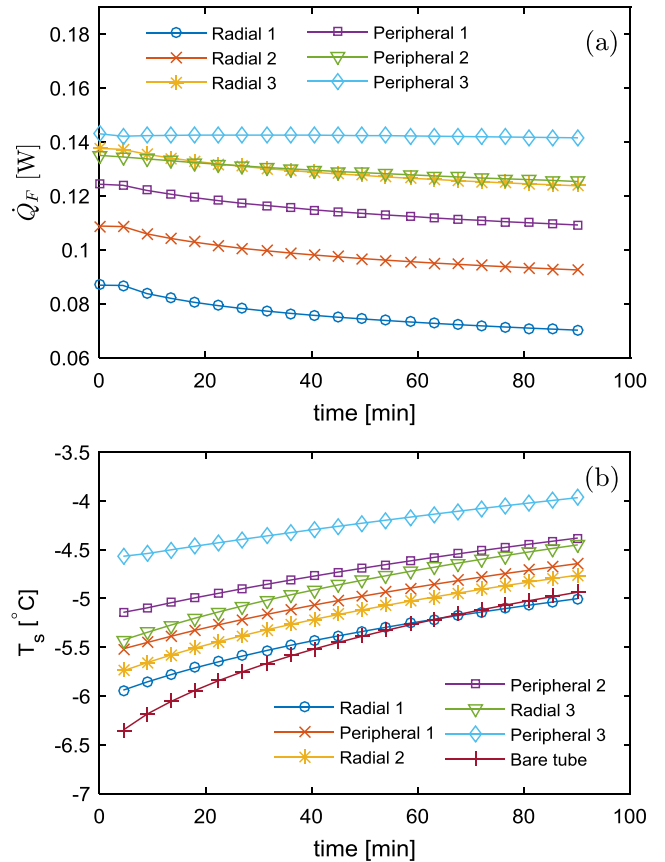


Fig. 19. (a) Heat transfer rate (CV1) and (b) frost surface temperature (CV5) as function of time for each extended surface type. Experimental conditions: (a) air flow rate: 34.4 m³/h; $T_{c,in} = -10.4$ °C; $\phi_{in} = 80.2\%$; $T_{a,in} = 14.8$ °C; test duration: 90 min.

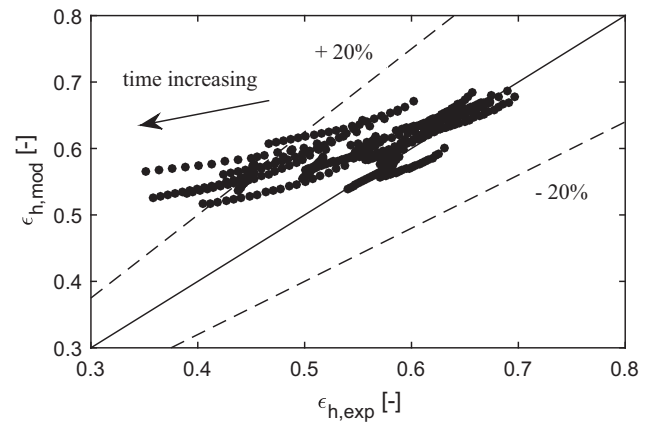


Fig. 20. Comparison between the model predictions and experimental enthalpy effectiveness results for the entire data set.

Fig. 19(a) presents, for a typical test condition, the heat transfer rate calculated by the model for each fin type, in the first control volume (CV1). The heat transfer rate is higher in the peripheral fins than in the radial fins of each level. Also, a higher heat transfer rate is observed in level 3 due to its larger area, which decreases until level 1. This is consistent with the analysis of Ref. [7], where the heat transfer was predicted to be more intense in the peripheral than in the radial fins. The frost surface temperature behavior for the same test condition (in the fifth control volume, CV5) is shown in Fig. 19(b).

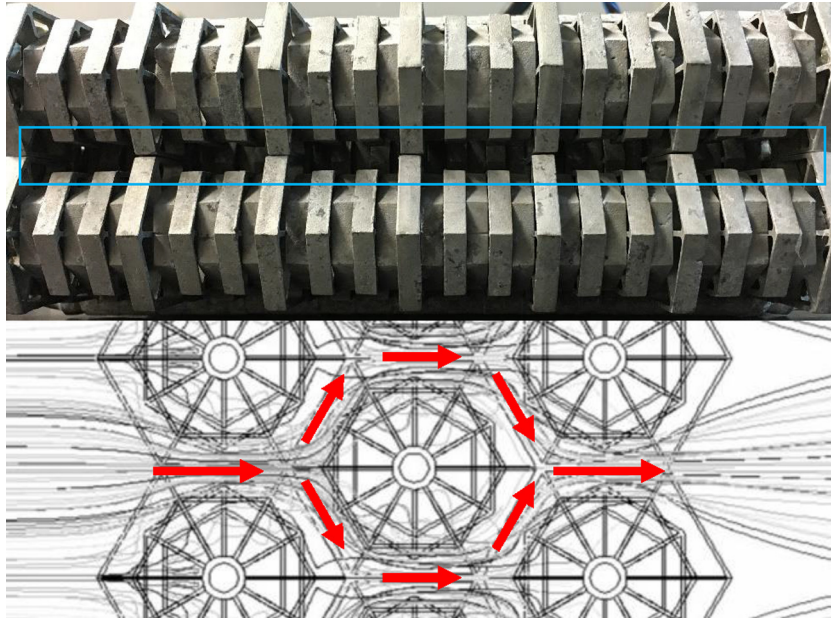


Fig. 21. Change of the flow path due to frost thickening (adapted from [7]).

The overall heat transfer rate prediction considering the entire data set is presented in terms of the enthalpy effectiveness, ϵ_h , defined as the ratio of the actual heat transfer rate (sensible and latent) and the maximum heat transfer rate as follows:

$$\epsilon_h = \frac{\dot{Q}}{\dot{m}_a(h_{a,in,hx} - h_{a,min,hx}) - \dot{m}_a(\omega_{a,in,hx} - \omega_{min,hx})h_{s,T_c}}, \quad (25)$$

where $h_{a,min,hx}$ is the minimum possible moist air enthalpy at the heat exchanger outlet and $\omega_{min,hx}$ is the humidity ratio of saturated air if it were at the inlet coolant temperature, $T_{c,in}$. h_{s,T_c} is the enthalpy of the frost layer at $T_{c,in}$.

Fig. 20 presents the experimental and calculated results in terms of the enthalpy effectiveness, for the entire data set. As can be observed, the model and the experimental data agree satisfactorily at the earlier times (when the frost thickness is small), which is consistent with the findings of [8] for purely sensible heat transfer in PFT heat exchangers. However, for some test conditions, much larger deviations were observed during the final stages of the tests. These may be due to a number of reasons. Firstly, at the later stages of the frost formation, the calculated frost surface temperature is higher than the highest temperature in the range of validity of the frost density correlation [15], i.e., -18.6°C to -5°C . This can affect not only the accuracy of the prediction of the frost thickness, but also the estimation of the frost thermal conductivity itself, which also depends on the choice of a specific correlation [19]. Secondly, as the frost thickness is supposedly under predicted and the flow passages across the radial fins are actually more obstructed by the frost than what the model estimates, the model gradually loses the ability of accurately predicting the reduction of the effective heat transfer surface area. As a result, the heat transfer rate (and the enthalpy effectiveness) is over predicted.

Lastly, as the model considers the heat exchanger a homogeneous porous medium, it cannot predict the appearance of preferential flow paths in the matrix, which are caused by a non-homogeneous frost growth on the fin surfaces. As a result, a larger fraction of the air flows through the larger spaces between the fin rows (as illustrated in Fig. 21) due to frost thickening near the tubes. In reality, as the effective surface area associated with the radial fins is reduced, the parallel-flow channels between the smaller fins become the primary flow path. The fact that this path

is the least thermally effective is another reason for the reduction of the heat transfer rate observed experimentally, increasing the prediction error even more.

5. Conclusions

A thermal analysis of the peripheral finned-tube geometry under frosting conditions was developed in this paper. A wind-tunnel calorimeter was used to evaluate the performance of a prototype developed by Pussoli et al. [8] at twenty-four different test conditions. Parameters such as the total heat transfer rate, pressure drop and frost accumulation were acquired. Detailed mathematical models were developed to predict the heat transfer in the fins, the moist air enthalpy and air humidity ratio variation along the heat exchanger and the frost growth on the enhanced surfaces. As expected, frost accumulation was most severe at air inlet, with noticeably less frost downstream. Also, an uneven frost accumulation was observed along the tubes, for each tube pass. While both effects increase the overall pressure drop, they moderate the overall effect of the frost thermal resistance.

A satisfactory agreement was found between the model predictions and the experimental data, with most of the data for the mass of frost, pressure drop and enthalpy effectiveness lying within $\pm 20\%$ error. The enthalpy effectiveness was observed to drop from 0.68 for dry to 0.50 under severe frosting, which suggests the PFT heat exchanger continued to be effective even under frost.

Acknowledgements

This work was made possible through the financial investment from the EMBRAPPII Program (POLO/UFSC EMBRAPPII Unit - Emerging Technologies in Cooling and Thermophysics). In addition, financial supports from Embraco and CNPq (Grant No. 573581/2008-8 - National Institute of Science and Technology in Cooling and Thermophysics) are duly acknowledged.

Conflict of interest

There is no actual or potential conflict of interest including any financial, personal or other relationships with other people or

organizations within three years of beginning the submitted work that could inappropriately influence, or be perceived to influence, the present work.

References

- [1] M. Kim, H. Kim, K. Lee, D.R. Kim, Frosting characteristics on hydrophobic and superhydrophobic surfaces: a review, *Energy Convers. Manage.* 138 (2017) 1–11.
- [2] Z. Zuo, R. Liao, X. Zhao, X. Song, Z. Qiao, C. Guo, A. Zhuang, Y. Yuan, Anti-frosting performance of superhydrophobic surface with ZnO nanorods, *Appl. Therm. Eng.* 110 (2017) 39–48.
- [3] P.W. Wilson, W. Lu, H. Xu, P. Kim, M.J. Kreder, J. Alvarenga, J. Aizenberg, Inhibition of ice nucleation by slippery liquid-infused porous surfaces (SLIPS), *Phys. Chem. Chem. Phys.* 15 (2013) 581–585.
- [4] P. Irajizad, M. Hasnain, N. Farokhnia, S.M. Sajadi, H. Ghasemi, Magnetic slippery extreme icephobic surfaces, *Nat. Commun.* 7 (2016) 13395.
- [5] M. Elsharkawy, D. Tortorella, S. Kapatral, C.M. Megaridis, Combating frosting with Joule-heated liquid-infused superhydrophobic coatings, *Langmuir* 32 (2016) 4278–4288.
- [6] M. Amer, C.-C. Wang, Review of defrosting methods, *Renew. Sust. Energy Rev.* 73 (2017) 53–74.
- [7] H. Wu, D. Ma, M. Kaviany, Peripheral fins for blockage robustness, *Int. J. Heat Mass Transfer* 50 (2007) 2514–2520.
- [8] B.F. Pussoli, J.R. Barbosa, L.W. da Silva, M. Kaviany, Heat transfer and pressure drop characteristics of peripheral-finned tube heat exchangers, *Int. J. Heat Mass Transfer* 55 (2012) 2835–2843.
- [9] S. Whitaker, Forced convection heat transfer correlations for flow in pipes, past flat plates, single cylinders, single spheres, and for flow in packed beds and tube bundles, *AIChE J.* 18 (1972) 361–371.
- [10] D. Handley, P.J. Heggs, Momentum and heat transfer mechanisms in regular shaped packings, *Trans. Inst. Chem. Eng.* 46 (1968) T251.
- [11] S.S. Ergun, Fluid flow through packed columns, *Chem. Eng. Prog.* 48 (1952) 89–94.
- [12] A. Montillet, E. Akkari, J. Comiti, About a correlating equation for predicting pressure drops through packed beds of spheres in a large range of Reynolds numbers, *Chem. Eng. Proc.* 46 (2007) 329–333.
- [13] B.F. Pussoli, J.R. Barbosa, L.W. da Silva, M. Kaviany, Optimization of peripheral finned-tube evaporators using entropy generation minimization, *Int. J. Heat Mass Transfer* 55 (2012) 7838–7846.
- [14] R.L. Webb, N.-H. Kim, *Principles of Enhanced Heat Transfer*, CRC Press, 2005.
- [15] Y. Hayashi, A. Aoki, S. Adashi, K. Hori, Study of frost properties correlating with frost formation types, *ASME J. Heat Transfer* 99 (1977) 239–245.
- [16] J. Iragorry, Y.X. Tao, S. Jia, A critical review of properties and models for frost formation analysis, *HVAC & R Res.* 10 (2004) 393–420.
- [17] C.J.L. Hermes, F.R. Loyola, V.S. Nascimento, A semi-empirical correlation for the frost density, *Int. J. Refrig.* 46 (2014) 100–104.
- [18] S. Negrelli, C.J.L. Hermes, A semi-empirical correlation for the thermal conductivity of frost, *Int. J. Refrig.* 58 (2015) 243–252.
- [19] K.S. Lee, W.S. Kim, T.H. Lee, A one-dimensional model for frost formation on a cold flat surface, *Int. J. Heat Mass Transfer* 40 (1997) 4359–4365.
- [20] B. Na, R. Webb, New model for frost growth rate, *Int. J. Heat Mass Transfer* 47 (2004) 925–936.
- [21] C.J.L. Hermes, R.O. Piucco, J.R. Barbosa, C. Melo, A study of frost growth and densification on flat surfaces, *Exp. Therm. Fluid Sci.* 33 (2009) 371–379.
- [22] J. Hwang, K. Cho, Numerical prediction of frost properties and performance on fin-tube heat exchanger with plain fin under frosting, *Int. J. Refrig.* 46 (2014) 59–68.
- [23] F.T. Knabben, C.J.L. Hermes, C. Melo, Numerical assessment of frosting and defrosting of no-frost evaporators, in: J.E. Braun (Ed.), *Proceedings of the Thirteenth International Refrigeration and Air Conditioning Conference at Purdue, West Lafayette, IN, 2010*, paper 2111, 2011.
- [24] D.L. Silva, C.J.L. Hermes, C. Melo, First principles modeling of frost accumulation on fan supplied tube fin evaporators, *Appl. Therm. Eng.* 31 (2011) 2616–2621.
- [25] Y.-G. Chen, Q.-Y. Jiang, J.-C. Yang, J.-X. Hou, X.-Y. Wu, Modeling and performance analyses of fin-and-tube heat exchanger operating under frost conditions, *Int. J. Low-Carbon Technol.* 12 (2017) 162–170.
- [26] C.J.L. Hermes, An analytical solution to the problem of frost growth and densification on flat surfaces, *Int. J. Heat Mass Transfer* 55 (2012) 7346–7351.
- [27] X. Wu, Q. Ma, F. Chu, Numerical simulation of frosting on fin-and-tube heat exchanger surfaces, *J. Therm. Sci. Eng. Appl.* 9 (2017) 031007.
- [28] D. Seker, H. Karatas, N. Egrican, Frost formation on fin-and-tube heat exchangers. Part I: Modeling of frost formation on fin-and-tube heat exchangers, *Int. J. Refrig.* 27 (2004) 367–374.
- [29] D.K. Yang, K.S. Lee, S. Song, Modeling for predicting frosting behavior of a fin-tube heat exchanger, *Int. J. Heat Mass Transfer* 49 (2006) 1472–1479.
- [30] D.L. Silva, C.J.L. Hermes, C. Melo, Experimental study of frost accumulation on fan-supplied tube-fin evaporators, *Appl. Therm. Eng.* 31 (2011) 1013–1020.
- [31] M.A.S. Timmermann, *Frost Formation in Peripheral Finned Tube Heat Exchangers*, Master's thesis, Universidade Federal de Santa Catarina, 2016.
- [32] J. Barbosa, R.A. Sigwalt, Air-side heat transfer and pressure drop in spiral wire-on-tube condensers, *Int. J. Refrig.* 35 (2012) 939–951.
- [33] J.L. Threlkeld, T.H. Kuehn, J.W. Ramsey, *Thermal Environmental Engineering*, Prentice Hall, 1998, ISBN 9780139172205.
- [34] R. Shah, D. Sekulic, *Fundamentals of Heat Exchanger Design*, Wiley, 2003, ISBN 9780471321712.
- [35] D. Spalding, *Convective Mass Transfer*, Hodder & Stoughton Ed., 1963.
- [36] X. Wu, F. Chu, Q. Ma, Frosting model based on phase change driving force, *Int. J. Heat Mass Transfer* 110 (2017) 760–767.
- [37] K.S. Lee, S. Jhee, D.K. Yang, Prediction of the frost formation on a cold flat surface, *Int. J. Heat Mass Transfer* 46 (2003) 3789–3796.
- [38] S.A. Klein, F.L. Alvarado, EES, *F-Chart Software, Professional Version 10*, 2015.
- [39] P.L. Brian, R.C. Reid, Y.T. Shah, Frost deposition on cold surfaces, *Ind. Eng. Chem. Fund.* 9 (1970) 375–380.
- [40] J. Shin, A. Tikhonov, C. Kim, Experimental study on frost structure on surfaces with different hydrophilicity: density and thermal conductivity, *J. Heat Transfer* 125 (2003) 84–94.
- [41] D.K. Yang, K.S. Lee, S. Song, Fin spacing optimization of a fin-tube heat exchanger under frosting conditions, *Int. J. Heat Mass Transfer* 49 (2006) 2619–2625.
- [42] C. Tso, Y. Cheng, A. Lai, Dynamic behavior of a direct expansion evaporator under frosting condition. Part I. Distributed model, *Int. J. Refrig.* 29 (2006) 611–623.
- [43] A. Cheikh, A. Jacobi, A mathematical model for frost growth and densification on flat surfaces, *Int. J. Heat Mass Transfer* 77 (2014) 604–611.
- [44] V.S. Nascimento, F.R. Loyola, C.J.L. Hermes, A study of frost build-up on parallel plate channels, *Exp. Therm. Fluid Sci.* 60 (2015) 328–336.